

1 Photoluminescent 1–2 nm Sized Silicon Nanoparticles: A Surface- 2 Dependent System

3 Juan J. Romero,[†] Manuel J. Llansola-Portolés,^{†,§} María Laura Dell’Arciprete,[†] Hernán B. Rodríguez,[†]
4 Ana L. Moore,[‡] and Mónica C. Gonzalez^{*,†}

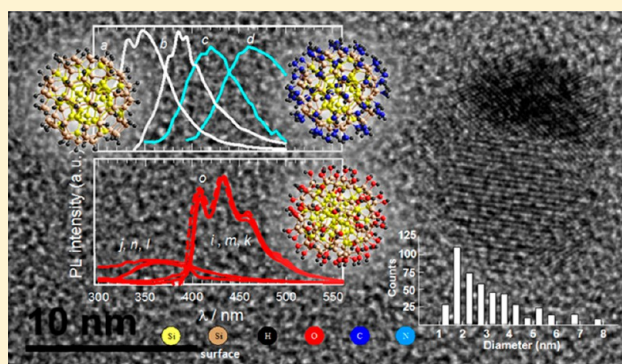
5 [†]Instituto de Investigaciones Fisicoquímicas Teóricas y Aplicadas (INIFTA), Facultad de Ciencias Exactas, Universidad Nacional de
6 La Plata, Casilla de Correo 16, Sucursal 4, (1900) La Plata, Argentina

7 [‡]Department of Chemistry and Biochemistry, Center for Bioenergy and Photosynthesis, Arizona State University, Tempe, Arizona
8 85287-1604, United States

9 **S** Supporting Information

10 **ABSTRACT:** The effect of derivatization and temperature on
11 the photoluminescence of 1–2 nm size silicon particles of
12 different origin is investigated in an attempt to understand the
13 effect of surface on the particles’ photoluminescence. To this
14 purpose, silicon nanoparticles were synthesized by electro-
15 chemical (top-down) and wet chemical (bottom-up) procedures.
16 Further derivatization by silylation or sylanization yielded
17 particles with $\equiv\text{Si}-\text{C}\equiv$, $\equiv\text{Si}-\text{O}-\text{Si}\equiv$, and $\equiv\text{Si}-\text{O}-$
18 $\text{C}\equiv$ groups at the interface. A detailed analysis of the
19 corresponding excitation–emission matrices strongly indicates
20 that different surface atomic arrangements contribute to the
21 energy gap. In particular, particles with $\equiv\text{Si}-\text{O}-\text{Si}\equiv$ groups
22 at the interface show photoluminescence independent of the
23 crystalline structure and on their further surface derivatization with different organic molecules. The lifetime and spectrum shape
24 of all synthesized particles are invariable to changes in temperature in the range 270–330 K despite a significant reduction in the
25 photoluminescence intensity being observed with increasing temperature; such behavior supports a thermal equilibrium between
26 dark and bright conformations of the particles. The observed results are of importance for optimizing the use of silicon
27 nanoparticles as optical sensors and therapeutic agents in biological systems.

28 **KEYWORDS:** surface states, thermal quenching, Si/SiO₂ interface, optical properties, surface chemistry



29 ■ INTRODUCTION

30 Silicon nanoparticles of 1–5 nm size (SiNPs) have received
31 great attention as they combine photoluminescence emission
32 (PL) spanning the visible and near-IR spectral region, with the
33 capability for singlet oxygen (¹O₂) and superoxide (O₂^{•-})
34 generation.^{1,2} Remarkable properties of nanostructured silicon
35 are their biocompatibility, biodegradability, and tunable surface
36 derivatization for drug delivery.^{3,4} SiNPs surface derivatization
37 with active functional groups, biomolecules, and biocompatible
38 polymers is a key step in the development of their many
39 technological applications. An adequate selection of the surface
40 groups renders the particles’ special properties as dispersibility
41 in the desired medium, surface protection against oxidation,
42 specific targeting, and opsonin association prevention.⁵
43 Work with SiNPs has shown that crystallinity, surface
44 structure, and surface chemistry play a role in their photo-
45 physical behavior. Interpreting and classifying the large number
46 of energy gaps (EG) and Stokes shifts (SS) reported for SiNPs
47 is difficult due to long-standing divergences in the synthesis of
48 monodisperse samples with well-characterized surfaces, as a
49 variety of groups (e.g., $\equiv\text{Si}-\text{OH}$, $>\text{Si}=\text{O}$, $\equiv\text{Si}-\text{O}-\text{Si}\equiv$,

$\equiv\text{Si}-\text{H}$, $\equiv\text{Si}-\text{C}\equiv$, etc.) present in different proportions 50
may form the interface of the designed product. In fact, the 51
fundamental photophysics of SiNPs is not currently as well 52
understood as that of direct gap semiconductors such as CdSe. 53

Electron density functional theory assuming finite barrier for 54
the potential confinement applied to H-saturated silicon 55
clusters predicts smooth variations of the EG with size. 56
Increased EG observed experimentally for crystalline clusters 57
were suggested to be a consequence of symmetry and reduced 58
angular distortion in the Si–Si bonds.⁸ These authors 59
predicted that localization of the HOMO and the LUMO 60
occurred throughout the core for unreconstructed surfaces 61
(e.g., Si₃₅H₃₆ bulk surface) whereas localization at the surface 62
was observed for reconstructed surfaces (e.g., Si₂₉H₂₄). 63
Moreover, experimental and computational work with SiNPs 64
demonstrated the fundamental importance of surface chemistry 65
in dictating their photophysical behavior.^{6,9,10} In particular, 66

Received: May 23, 2013

Revised: August 2, 2013

single bonded Si—OH and Si—O—Si groups on Si₂₉ and Si₄₇ cores have relatively slight influences on the band edges and gap, whereas double bonded Si=O surface structures significantly affect them. The increase in surface coverage causes a further change of the EG.⁹ More recent studies suggest that Si—O—Si structures on the curved surface of <3 nm size SiNPs, but not on the facet of >3–4 nm particles, lead to localized levels in the EG. As a consequence, a red-shift in the PL spectra of small oxidized SiNPs is observed.¹¹

The temperature dependence of the PL of SiNPs is suggested to be an intrinsic property of the particles strongly depending on size.^{12–14} SiNPs from different synthesis routes are reported to show increased PL intensity with decreasing temperature until ca. 60–80 K. A further decrease in temperature rapidly diminishes the PL intensity along with an increased PL lifetime. These observations are discussed in terms of the competition between temperature-dependent radiative (k_r) and nonradiative ($\sum_i k_{ni}$) decay rates of the highly localized excitons, as those provided by defects in the nanocrystal or at the Si/SiO₂ interface.

Herein we investigate the effect of surface derivatization and temperature on the PL of SiNPs of different origin in an attempt to understand the effect of surface on the particles PL. This knowledge is necessary for optimizing the use of SiNPs as optical sensors and therapeutic agents in biological systems. To that purpose, SiNPs were synthesized by electrochemical (top-down, TD) and wet chemical procedures (bottom-up, BU), and further derivatized by silylation or silyanization to yield particles with —NH₂ terminal groups and different chemistry at the interface ($\equiv\text{Si—C}\equiv$, $\equiv\text{Si—O—Si}\equiv$, and/or $\equiv\text{Si—O—C}\equiv$).

EXPERIMENTAL SECTION

Materials. Toluene (99.7%, H₂O 0.005%), methyl 2-methylprop-2-enoate, methanol, cyclohexane, 9,10-diphenylanthracene, LiAlH₄ (95%), SiCl₄ (99%), ethyl ether (p.a. 99.9%), tetraoctylammonium bromide (98%), (3-aminopropyl)triethoxysilane, and 2-propen-1-amine were purchased from Sigma-Aldrich and employed without further purification. Deionized water (>18 M Ω cm, <20 ppb of organic carbon) was obtained with a Millipore system. Nitrogen (4 bands quality) and oxygen gas were both from La Oxigena S.A., Argentina.

Equipment. FTIR spectra were obtained with a Bruker EQUINOX spectrometer. Either KBr disks or silicon wafers were used as holders. Spectra were taken in the 4000–400 cm⁻¹ range with 1 cm⁻¹ resolution. Attenuated total reflection infrared (ATR-IR) spectroscopy used for the analysis of the surface of derivatized particles was performed with a Nicolet 380 FTIR ATR accessory using a ZnSe crystal and an incident beam angle of 45°.

The attenuation spectra were recorded with a double-beam Shimadzu UV-1800 spectrophotometer in a 1 cm quartz cuvette at a scan rate of 300 nm/min. The nanoparticle light scattering is calculated by fitting the 450–800 nm range attenuation to a $a \times \lambda^{-4}$ dependence. The corrected absorbance spectrum is obtained by subtraction of the scattering from the measured attenuation spectrum.

PL measurements were performed with a Jobin-Yvon Spex Fluorolog FL3-11 spectrometer. The fluorimeter is equipped with a Xe lamp as the excitation source, a monochromator with 1 nm bandpass gap for selecting the excitation and emission wavelengths, and a red sensitive R928 p.m. as detector. All spectra were corrected for the wavelength-dependent sensitivity of the detector and the source. Additionally, emission spectra were corrected for Raman scattering by using the solvent emission spectrum. To estimate the emission quantum yield (Φ), emission spectra were collected at various excitation wavelengths. Identical measurements (excitation conditions, lamp energy, and spectrometer band-pass) were performed on 9,10-diphenylanthracene in cyclohexane.^{2,15,16} The temperature

was controlled to ± 0.1 °C with an F-3004 Peltier sample cooler controlled by a LFI-3751 temperature controller (Wavelength electronics).

Time-resolved PL measurements were performed with either a Jobin-Yvon Spex Fluorolog FL3-11 spectrometer (vide supra) equipped with TCSPC with LED excitation at 341 and 388 nm (fwhm \sim 400 ps) or a mode-locked Ti:Sapphire laser (Spectra Physics, Millennia-pumped Tsunami) with a 130-fs pulse duration operating at 80 MHz. The laser output was sent through a frequency doubler and pulse selector (Spectra Physics Model 3980) to obtain 370–450 nm pulses at 4 MHz. Fluorescence emission was detected at the magic angle using a double grating monochromator (Jobin Yvon Gemini-180) and a microchannel plate PMT (Hamamatsu R3809U-50). The instrument response function was 35–55 ps. Data was acquired by a Becker-Hickl SPC-830 card. Temperature was controlled to ± 0.1 °C with an Oxford Optistat DN liquid nitrogen-cooled optical cryostat equipped with an Oxford ITC 601 controller. Data was globally fitted as sum of exponentials including IRF deconvolution until optimal values of χ^2 , residuals, and standard deviation parameters were attained.

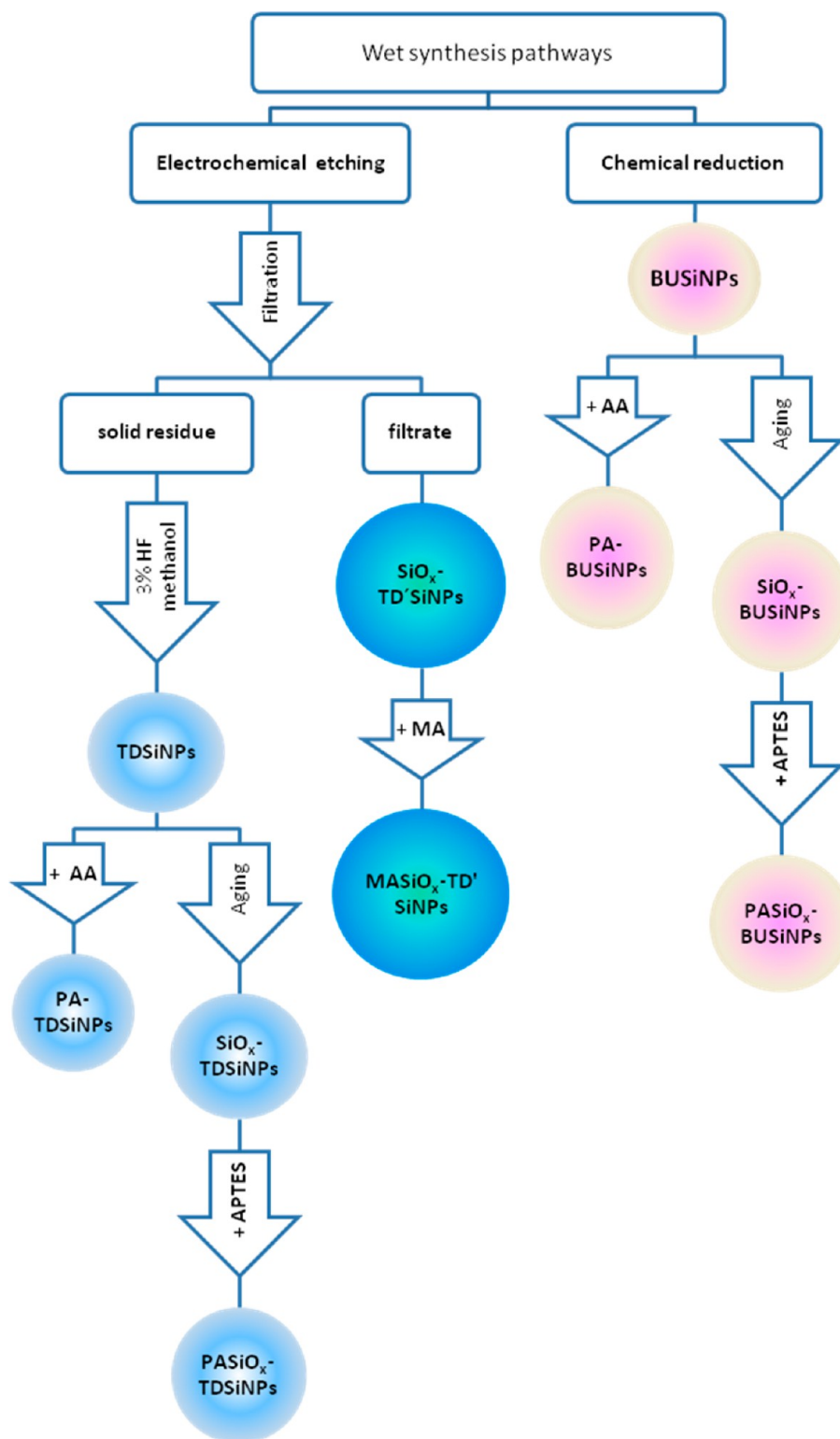
TEM micrographs were taken with a JEOL 2010 F microscope using a carbon-coated 300-mesh copper grid. Images were analyzed employing the Image Tool 3.0 software (Health Science Center of the University of Texas, San Antonio, TX, USA). Particle diameters were determined assuming that the particle area obtained from the TEM images is the projection of a spherical particle. A log-normal function was found to best describe the size distribution of the 500 particles sample.

The X-ray photoelectron spectroscopy (XPS) spectra were obtained under UHV with a XR50 Specs GmbH spectrometer with Mg K α as the excitation source and a PHOIBOS 100 half sphere energy analyzer. Internal calibration was performed with Au 4f_{7/2} (binding energy, BE, 84.00 eV) and with the C 1s peak at BE = 284.6 eV due to adventitious carbon. Also, to get a better insight into the chemical environment of the different atoms, high resolution XPS spectra were taken and resolved by Gaussian–Lorentzian fitting, keeping χ^2 values between 1 and 1.25.

Bilinear Regression Analysis. For low fluorophore absorbance (<0.05), the steady state emission intensity at the given emission wavelength, $I(\lambda_{em})$, is proportional to the absorption coefficient of the fluorophore at the excitation wavelength, $\epsilon(\lambda_{ex})$, the concentration of the fluorophore, and a factor $F(\lambda_{em})$ reflecting the shape of the emission spectrum. The bilinear regression analysis takes advantage of the linearity of $I(\lambda_{em})$ with both $\epsilon(\lambda_{ex})$ and $F(\lambda_{em})$ to retrieve information from the experimental excitation–emission matrix on the minimum number of species and on their relative emission and absorption spectra.¹⁶ It should be noted that the recovery of the excitation–emission spectrum of all the individual components from a bilinear analysis of a multicomponent system is not always possible in those cases where the emission and excitation spectra of the different species are strongly superimposed.¹⁷ A further disadvantage is a low contribution of one of the species to the overall emission. In these cases, the different components may not be differentiated by a bilinear analysis, and the individual recovered species are rather a family of strongly optically related compounds.

SiNPs Synthesis. TD approaches involved an adaptation of the electrochemical method with HF etching of porous Si.¹ Briefly, clean crystalline Si wafers (p-type, with resistivity between 1.0 and 10.0 Ω cm) were electrochemically etched (20 mA electrical current) in a Teflon cell containing the electrolytic solution (16% HF, 16% CH₃OH v/v). After anodization, the wafer was rinsed with methanol and toluene, further immersed in Ar-saturated toluene, and Si-NP released by immersion in an ultrasound bath for 2 h (Ney Dental Inc.; 50/60 Hz; 100 W). The resulting suspension was purified by filtration through hydrophilic 100 nm PVDF membrane filters (MILLEX-HV, Millipore), and both the solid residue and the filtrate were separated to obtain different SiNPs.

The solid residue was suspended in a 3% HF methanol solution, sonicated, and stored in the dark for two hours to break up and etch agglomerates.¹⁸ After water addition, the well-dispersed aqueous 200

Scheme 1. Summary Flow Chart on the Synthesis Pathways Followed for Obtaining the Different SiNPs⁴

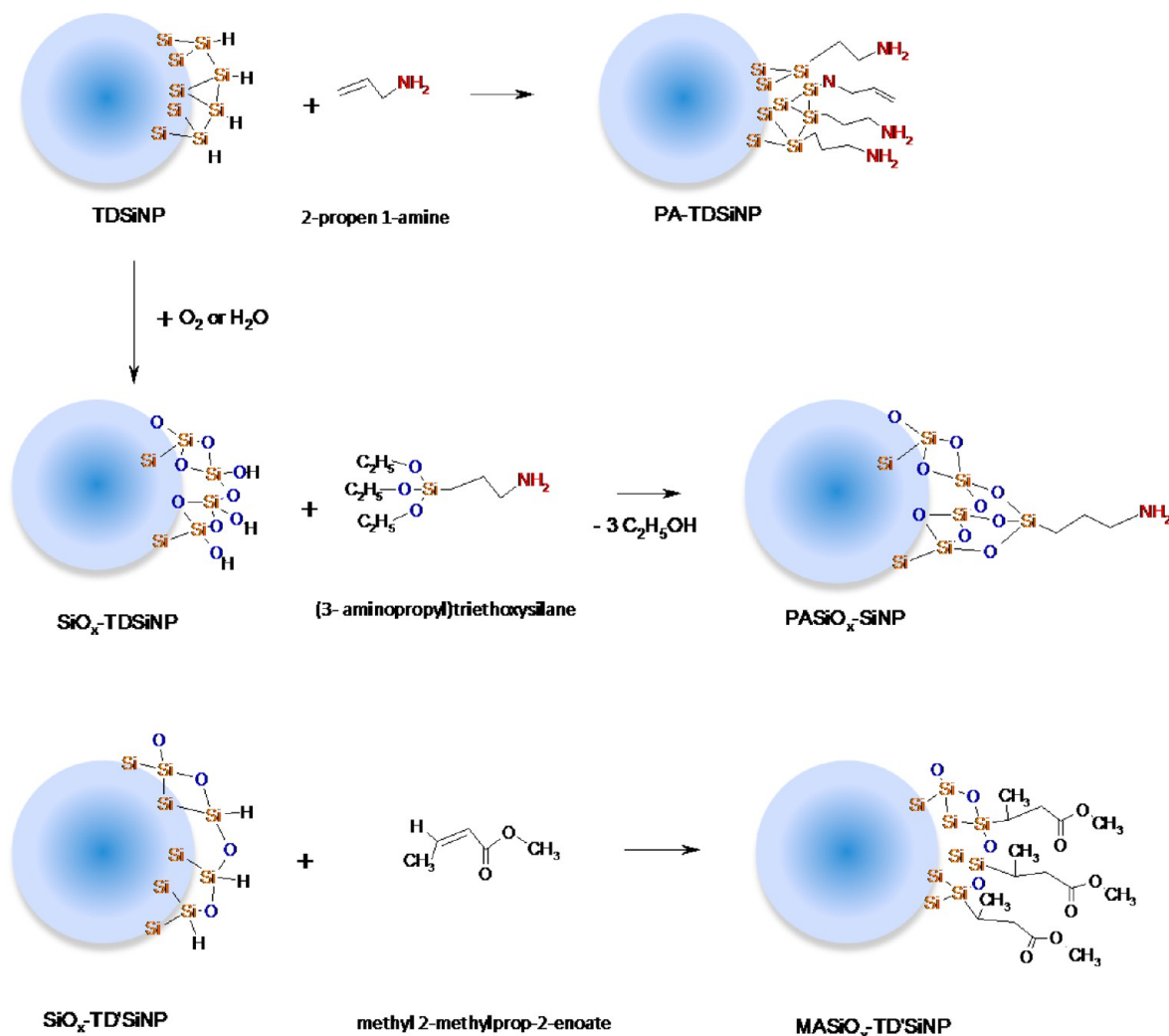
⁴AA, MA, and APTES stand for 2-propen 1-amine, methyl 2-methylprop-2-enoate, and (3-aminopropyl)triethoxysilane, respectively.

202 suspension of SiNPs was shaken with cyclohexane to extract the
203 hydrophobic nanoparticles with H-passivated surfaces to the organic
204 phase. The solvent was evaporated and the remaining silicon particles
205 dispersed in toluene for further use. The "as obtained" particles will be
206 referred to as TDSiNPs. When required, TDSiNPs were allowed to
207 age upon standing in an air-saturated suspension in the dark for several
208 weeks, leading to the formation of surface-oxidized particles, SiO_x-

TDSiNPs. Surface-oxidized 3 nm size SiNPs with a SiO_x layer and 209
Si—H surface functionalities are obtained from the filtrated 210
suspension.¹ Because of their common TD synthetic procedure, 211
these particles are referred to as SiO_x-TD'SiNPs. 212

The BU-approach synthesis involved an adaptation of the LiAlH₄ 213
reduction of SiCl₄ in the presence of tetraoctylammonium bromide 214
reversed micelles.¹⁶ Freshly prepared particles showing H- and Cl- 215

Scheme 2. Surface Composition of TDSiNPs Derivatized with 2-Propen 1-Amine and (3- Aminopropyl)triethoxysilane and TD'SiNPs derivatized with Methyl 2-Methylprop-2-enoate^a



^aThe blue circles stand for the silicon core of the particles.

216 passivated surfaces are named BUSiNPs. These surface groups are
 217 oxidized to Si—OH during storage under air-saturation for two weeks,
 218 as confirmed by the appearance of a broad band near 3400 cm⁻¹ in the
 219 FTIR spectrum, characteristic of Si—O—H stretching vibration. Aged
 220 particles are denoted as SiO_x-BUSiNPs.

221 **Surface Derivatization.** SiNPs were capped with organic
 222 molecules either by photoinitiated silylation or by thermal silanization.
 223 The silylation process involved mixing of a colloid dispersion of either
 224 fresh TDSiNPs or BUSiNPs in toluene with microliter quantities of 2-
 225 propen 1-amine (reactant in defect). The resulting suspension was
 226 irradiated for 5 h with 254 nm light from eight Rayonet Lamps
 227 (RPR2537A, Southern N.E. UltravioletCo.) to yield PA-TDSiNPs and
 228 PA-BUSiNPs. A similar procedure using 350 nm light from a Rayonet
 229 Lamp (RPR3500A, Southern N.E. UltravioletCo.) was applied for
 230 freshly prepared methyl 2-methylprop-2-enoate derivatized SiO_x-
 231 TD'SiNPs containing surface Si—H bonds (MASiO_x-TD'SiNPs).

232 The silanization procedure involved coupling of (3-aminopropyl)-
 233 triethoxysilane to terminal Si—OH groups.^{18,19} Therefore, suspended
 234 surface-oxidized BUSiNP and TDSiNP in toluene were treated with
 235 (3-aminopropyl)triethoxysilane and stirred at room temperature for 24
 236 h. Removal of excess organosilane and tetraoctylammonium bromide
 237 was achieved by membrane dialysis. Oxidized particles derivatized with
 238 (3-aminopropyl)triethoxysilane are referred to as PASiO_x-BUSiNPs
 239 and PASiO_x-TDSiNPs.

For clarity, a flowchart summary depicting the synthesis pathways is 240
 given in Scheme 1. 241 s1

RESULTS AND DISCUSSION 242

243 Silicon nanoparticles were obtained in the laboratory by top-
 244 down (TD) and bottom-up (BU) approaches, yielding H-
 245 passivated crystalline TDSiNPs and amorphous BUSiNPs with
 246 Si—H and Si—Cl surface groups, respectively (vide supra).
 247 These particles were either derivatized to cover the surface with
 248 propylamine terminal groups to yield PA-TDSiNPs and PA-
 249 BUSiNPs or allowed to age to yield surface oxidized SiO_x-
 250 TDSiNPs and SiO_x-BUSiNPs. The latter particles were further
 251 derivatized to yield propylamine-terminated PASiO_x-TDSiNPs
 252 and PASiO_x-BUSiNPs, respectively. SiO_x-TD'SiNPs particles
 253 were obtained by a modification of the TD approach involving
 254 the simultaneous oxidation and etching of porous silicon.¹ They
 255 differ from SiO_x-TDSiNPs in that they present Si—H, Si—
 256 O—Si, and Si—OH structures in their surface. SiO_x-TD'SiNPs
 257 particles were further derivatized to yield methyl 1-methyl-
 258 propanoate-terminated MASiO_x-TD'SiNPs. Scheme 2 summa-
 259 rizes the derivatization reactions for TDSiNPs and shows the
 260 average surface composition of the particles.

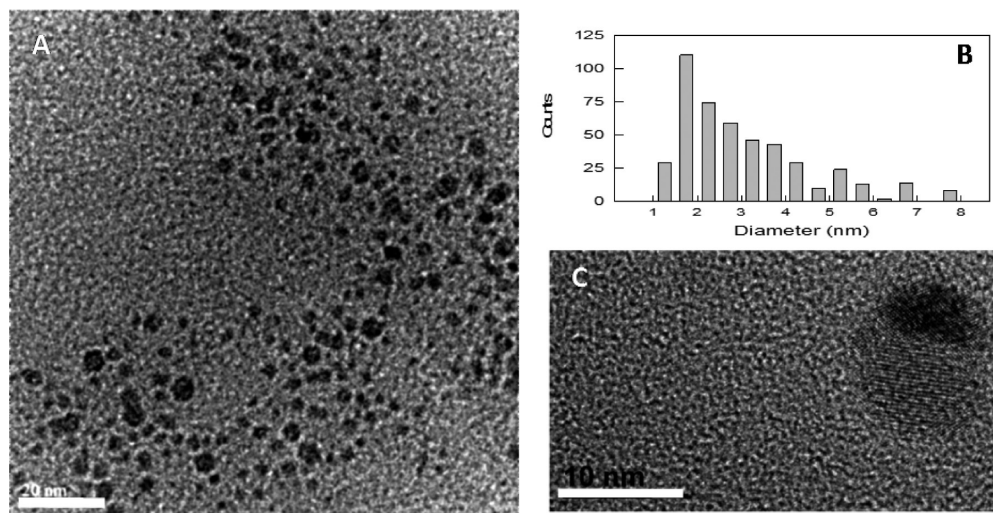


Figure 1. (A) TEM image of TDSiNPs, (B) associated size histogram of 500 non-touching particles, and (C) HRTEM micrograph of agglomerated particles showing silicon d_{111} crystalline planes.

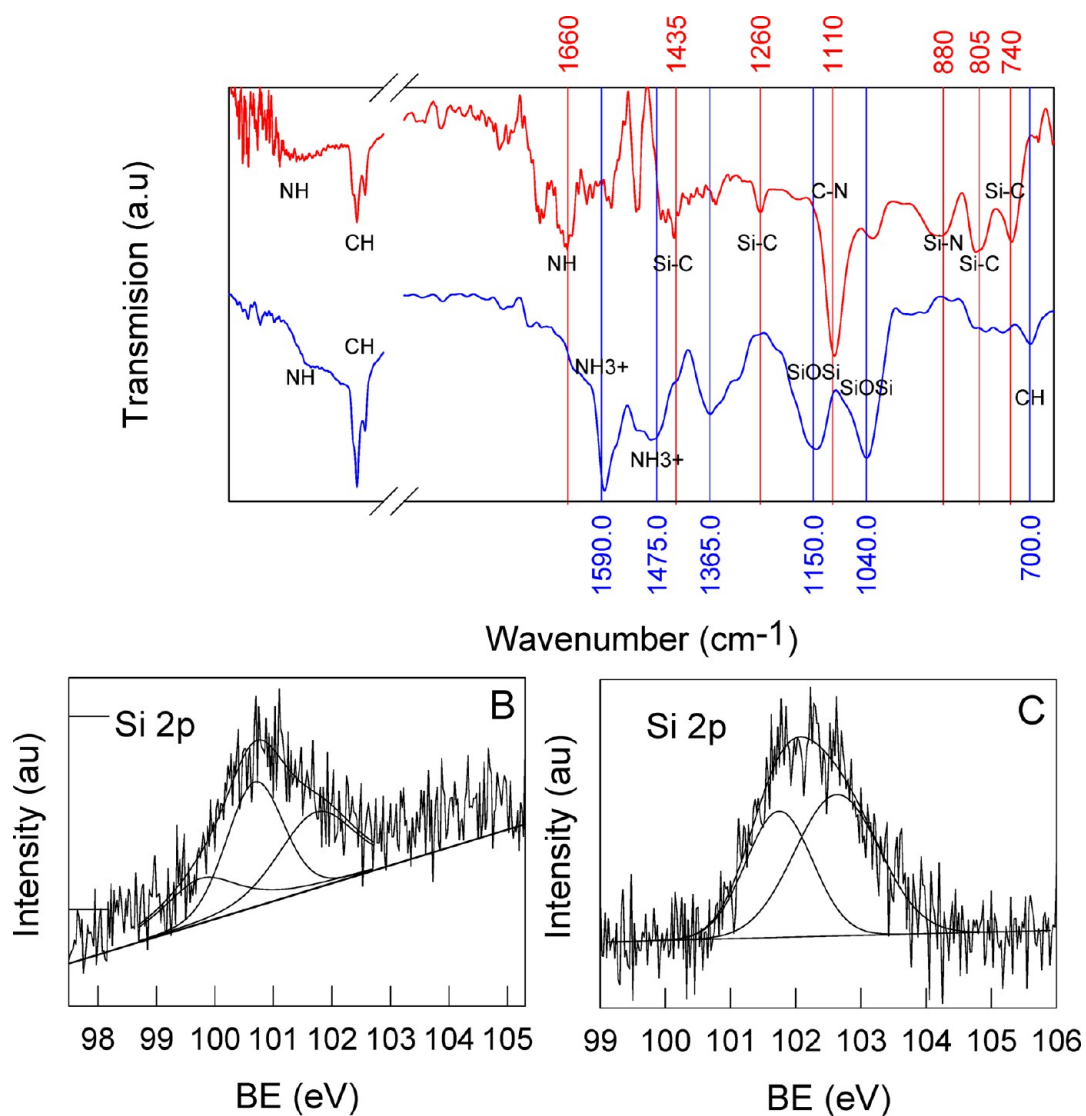


Figure 2. (A) FTIR spectra of PA-TDSiNPs (red spectrum) and $\text{PA-SiO}_x\text{-TDSiNPs}$ (blue spectrum), deposited from toluene suspensions on Si wafer supports. The vertical solid lines stand as guides to the eye for the peak positions. (B) and (C) stand for the high resolution Si 2p XPS peak of PA-TDSiNPs and $\text{PA-SiO}_x\text{-TDSiNPs}$, respectively.

Particle Characterization. An average size of 1.8 nm with a high dispersion toward bigger sizes is observed for TDSiNPs from the size histogram, as shown in Figure 1A,B. However, a thorough analysis of the micrographs (Figure 1C) indicates important particle agglomeration. In fact, atomic force microscopy performed on mercaptopropyl-derivatized TDSiNPs after drop-casting on a mica support and the heights extracted from scanning tunneling microscopy topography of mercaptopropyl-terminated TDSiNPs on a Au(111) substrate show size histograms indicating highly monodispersed samples with a mean particle height of (1.7 ± 0.3) and around (1.6 ± 0.5) nm, respectively.²⁰ The image in Figure 1C and other HRTEM micrographs shown in S.I. Characterization (Supporting Information) clearly show Si crystalline planes with lattice spacing of $3.1 \pm 0.1 \text{ \AA}$, in agreement with that reported for the d_{111} plane of SiNPs.^{21,22} On the other hand, aged BUSiNPs showed an average particle size of (1.7 ± 0.8) nm and no evidence of a crystalline structure could be found¹⁶ (see also TEM micrographs in S.I. Characterization, Supporting Information).

The analysis of the XPS and IR spectra of the different particles allows the determination of the average surface composition. Figure 2A, top spectrum, shows the FTIR spectrum of PA-TDSiNPs. The observed N–H vibrations in the 3400 (weak), 1650–1580, and 910–665 cm^{-1} regions are characteristic of primary and secondary amines. The C–N stretching vibration of aliphatic amines is observed at 1260 cm^{-1} . The presence of bands at 1435, 1270, 805, and 740 cm^{-1} due to Si–C symmetric and asymmetric deformation, stretching, and CH_2 rocking in Si– CH_2 respectively, as well as peaks in the 2970–2880 cm^{-1} region due to CH_2 stretching and bending, confirm PA bonding to TDSiNPs.^{23,24} The corresponding XPS spectrum shows Si 2p signals, Figure 2B, at 99.70 (10%), 100.7 (57%), and 101.8 eV (33%), characteristic of Si⁰, Si–C, and Si–N environments, respectively.^{25–27} The N 1s signal may be described by a main peak at 399.4 eV characteristic of C– NH_2 groups. No significant contribution due to N in Si environments (peak at 398 eV²⁷) is observed. However, the FTIR absorption at 880 cm^{-1} could be assigned to the presence of Si–N vibrations.²⁸ N-bonding to Si may be a secondary product of the radical mechanism involved in the synthesis reaction, as described in S.I. Scheme 1 (Supporting Information).

The FTIR spectra of PASiO_x-TDSiNPs, see bottom spectrum in Figure 2A, shows intense bands at 1150 and 1040 cm^{-1} characteristic of Si–O–Si in different environments, thus denoting surface-oxidized particles. Absorption bands in the region 1550–1450 cm^{-1} may be assigned to N–H vibrations in protonated amines.²⁹ The peak at 1332 cm^{-1} is assigned to CO_2 trapped by surface NH_3^+ in coincidence with that reported for protonated (3-aminopropyl)triethoxysilane films.³⁰ On the other hand, the Si 2p XPS peak displays the contribution of silicon environments with binding energies of 101.7 and 102.6 eV which may be assigned to Si(O–)₂ and Si(O–)₃–C environments,^{31,32} in agreement with the expected PASiO_x-TDSiNPs surface depicted in Scheme 2. N 1s peaks at 399.4 eV may be assigned to C– NH_2 environments, and the IR peaks due to CH_2 stretching and bending vibrations in the 2970–2880 cm^{-1} and 1465–1440 cm^{-1} region further support the covalent link of organic moieties to the silicon framework. The absence of Si 2p XPS peaks around 104 eV and IR bands around 1250 cm^{-1} due to

Si=O in bulk SiO₂ supports the negligible formation of SiO₂ structures.³³

Ratios between Si, O, C, and N signals in the XPS spectrum corrected for the instrument sensitivity yield the average surface composition for the different SiNPs, as shown in Table 1 and in

Table 1. Average Size and Surface Composition of Solid Samples Obtained from the Different Synthesis and Derivatization Procedures^a

particle	size, nm	average surface composition ^b
TDSiNPs	1.7 ± 0.3	-----
PA-TDSiNPs	1.7 ± 0.3	Si ₂ C ₃ N _{4.4} H _y
SiO _x -TDSiNPs	1.7 ± 0.3	-----
PASiO _x -TDSiNPs	1.7 ± 0.3	Si ₁₂ C _{3.5} H _y N ₁ O _x
MASiO _x -TD'SiNPs	3 ± 1 ^c	Si ₃ O ₆ (C ₅ O ₂ H _y) ₁ ^c
BUSiNPs	1.7 ± 0.8	-----
PA-BUSiNPs	1.7 ± 0.8	-----
SiO _x -BUSiNPs	1.7 ± 0.8	Si _{4.2} O _{3.8} ClH _y
PASiO _x -BUSiNPs	1.7 ± 0.8	-----

^aSurface oxidized particles are in bold. ^bH “y” proportion was not determined though observed. ^cData from ref 1.

agreement with the expected surface structures depicted in Scheme 2. FTIR and XPS characterization of BUSiNPs, PA-BUSiNPs, SiO_x-BUSiNPs, and PASiO_x-BUSiNPs also supports the expected surface structure, in agreement with the FTIR and XPS peak assignments observed for TDSiNPs derivatives. For further details refer to S.I. Characterization (Supporting Information). It should be recalled that PA-TDSiNPs also shows a small FTIR absorption at 850 cm^{-1} and peak contributions to the Si 2p band at 101.5 and 102.2 eV, characteristic of Si(C_xN_y) and Si–N environments.^{25,28} In conclusion, PA derivatization of H-passivated SiNPs by a photoinitiated radical mechanism leads invariably to N-bonding to Si independently of the crystalline structure of the silicon network.

Photoluminescence Experiments. The PL of the different particles in Ar-saturated toluene suspensions shows particular features strongly depending on surface groups and synthesis procedures. Moreover, the dependence of the emission spectrum with the excitation wavelength for a given suspension indicates the contribution of particles of different size, morphology, surface chemistry, and/or oxidation grade within the sample.¹⁶ The contribution of different emitters to the overall excitation–emission matrix was analyzed on the assumption that single chromophores existing in a unique form show excitation wavelength-invariant emission spectrum.¹⁶ Figure 3 shows the emission and excitation spectra of contributing emitters as obtained from the bilinear analysis of the excitation–emission matrix of argon-saturated toluene suspensions of the different synthesized particles.

Decay times (τ) and quantum yields at 298 K ($\Phi^{298\text{K}}$) were measured at selected excitation and emission wavelengths to focus on a particular contributing emitting species. Measured τ values for TDSiNPs and BUSiNPs and their surface-functionalized derivatives are within 1–7 ns, as depicted in Table 2. Under conditions of low excitation power density, the excited states of the particles decay unimolecularly and the PL quantum yield is $\Phi = k_r / (k_r + \sum_i k_{ni})$, where k_r stands for the radiative decay rate and $\sum_i k_{ni}$ for nonradiative processes. Therefore, considering the luminescence lifetime $\tau = (k_r + \sum_i k_{ni})^{-1}$, the product $\Phi \times \tau^{-1}$ yields k_r . Considering the data in Table 2, 367

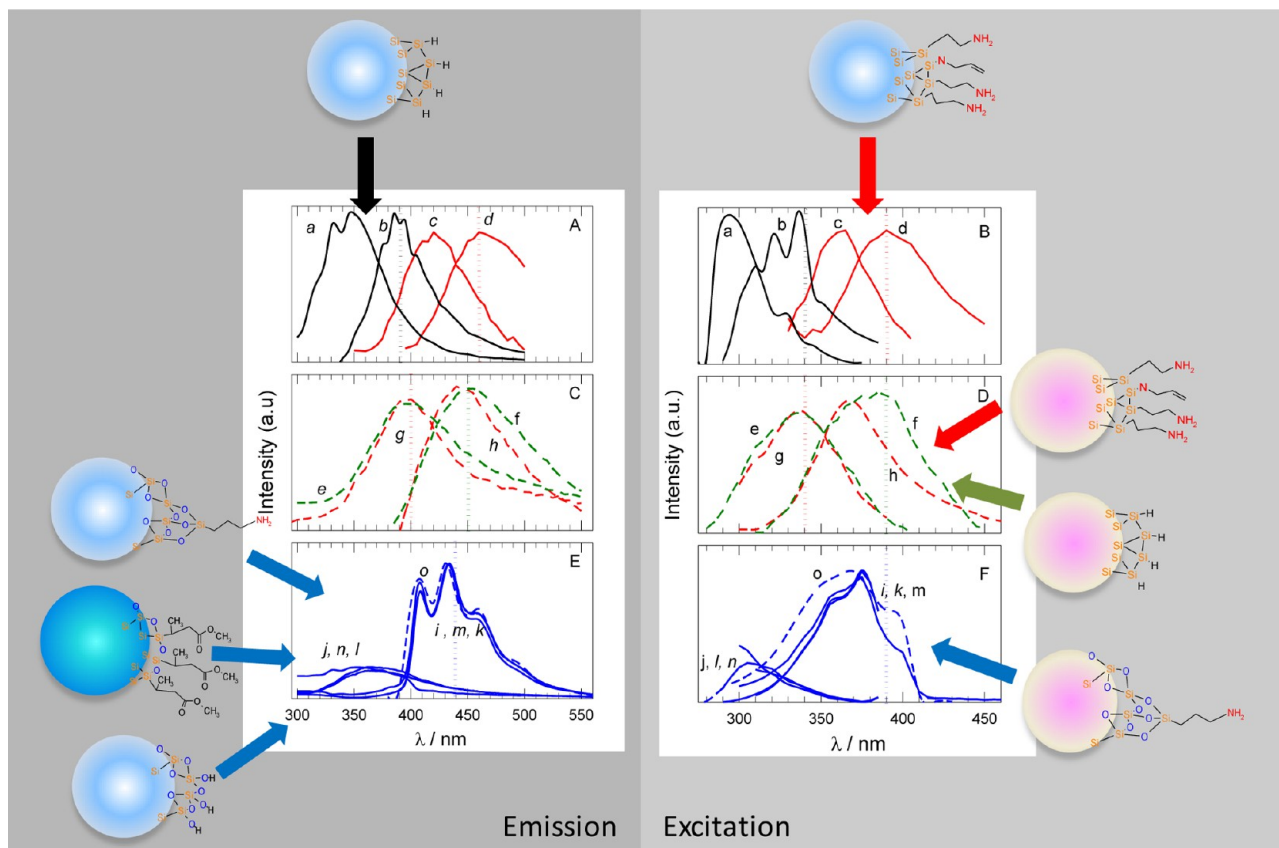


Figure 3. Emission (A, C, and E) and excitation (B, D, and F) spectra at 313 K of argon-saturated toluene suspensions of contributing emitters as obtained from the bilinear analysis of the excitation–emission matrix of TDSiNPs (*a* and *b*, black solid lines), PA-TDSiNPs (*c* and *d*, red solid lines), BUSiNPs (*e* and *f*, green dashed lines), PA-BUSiNPs (*g* and *h*, red dashed lines), SiO_x-TDSiNPs (*i* and *j*, blue solid lines), PASiO_x-TDSiNPs (*k* and *l*, blue solid lines), MASiO_x-TD'SiNPs (*m* and *n*, blue solid lines), and PASiO_x-BUSiNPs (*o*, blue dashed lines). The vertical lines stand for the excitation (B, D, and F) and detection (A, C, and E) wavelengths in time-resolved experiments.

Table 2. Energy gap (EG), maximum emission (λ_{em}^{max}), Stokes shifts (SS), decay times (τ), and quantum yields (Φ) of the different emitting particles obtained at 298 K in argon-saturated suspensions^a

particle	emitter	EG (± 0.05), eV	λ_{em}^{max} , eV	SS (± 0.05), eV	τ (%), ns	Φ^{298K} (± 0.05)
TDSiNPs	<i>a</i>	3.4	3.4	0.67	0.5 (76)	0.2 (air: 0.005)
	<i>b</i>	3.15	3.1	0.53	3.15 (19)	0.19
PA-TDSiNPs	<i>c</i>	3.0	2.95	0.49	1.6 \pm 0.1 (70)	0.16
	<i>d</i>	2.7	2.7	0.50	4.3 \pm 0.1 (27)	0.2 (air: 0.14)
SiO _x -TDSiNPs	<i>i</i>	3.0	3.0	0.45	1.27 \pm 0.05	0.13
	<i>j</i>	3.4	3.5	0.59	----	----
PA-SiO _x -TDSiNPs	<i>k</i>	3.0	3.0	0.45	1.30 \pm 0.05	0.36
	<i>l</i>	3.4	3.4	0.60	----	0.3
MASiO _x -TD'SiNPs ^b	<i>m</i>	3.0	2.85	0.43	1.19 \pm 0.05	0.76 (air:0.44)
	<i>n</i>	3.3	3.4	0.62	----	----
BUSiNPs	<i>e</i>	3.1	3.1	0.55	1.5 \pm 0.5	----
	<i>f</i>	2.8	2.8	0.45	7 \pm 0.5	----
PA-BUSiNPs	<i>g</i>	3.15	3.1	0.56	1.2 \pm 0.3 (80)	0.25
	<i>h</i>	2.65	2.75	0.63	4.5 \pm 0.1 (20)	0.34
SiO _x -BUSiNPs ^b		3.0	2.85	0.45	1.6 \pm 0.05	----
PASiO _x -BUSiNPs	<i>o</i>	2.95	2.85	0.44	1.1 \pm 0.1	0.1

^aDepicted Φ are lower limit values, see text. Values in bold stand for surface oxidized particles. ^bData from ref 16.

368 expected k_r values fall within $(1-60) \times 10^7 \text{ s}^{-1}$. However, as it
369 will be discussed later, Φ values also consider the absorbance of
370 dark particles, and therefore calculated k_r values are lower limit
371 estimations.

372 The mean energy gap (EG) of charge carriers in silicon
373 nanoparticles may be evaluated using the excitation spectrum

(PLE) threshold of each individual species.^{16,34} Calculated EG
374 values for each emitting species, shown in Table 2, coincide
375 with the PL maxima, strongly supporting that the excitation and
376 the emission mainly originate from the same transition.
377 Corresponding Stokes shifts (SS), also shown in Table 2,
378 vary within the 0.4–0.6 eV range.
379

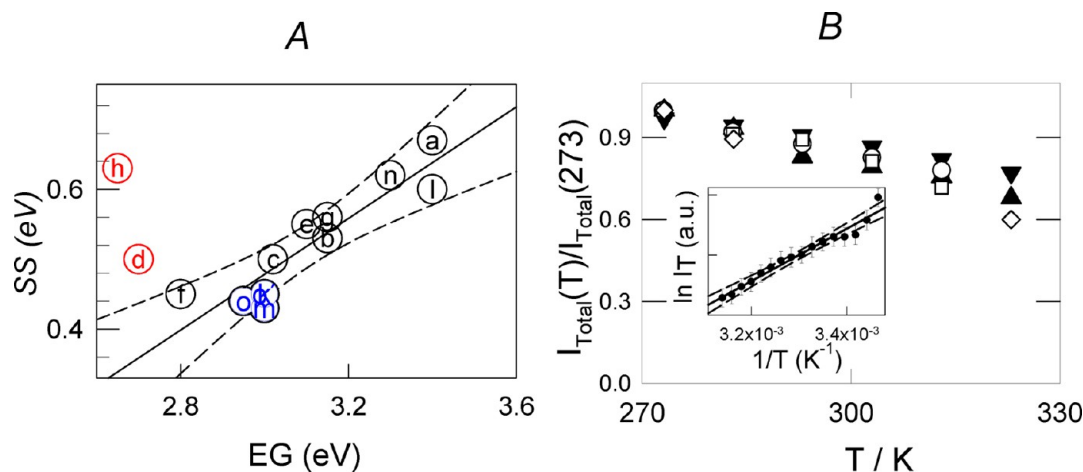


Figure 4. (A) Stokes distance dependence with the energy gap. The letters inside the symbols stand for the different emitting species. (B) Ratio of the total emission intensity at a given temperature to that observed at 273 K ($I_T(T)/I_T(273)$) for argon-saturated toluene suspensions of species *a* (\blacktriangledown), *b* (\blacktriangle), *c* (\diamond), *k* (\circ), and *m* (\square) vs T . Inset: $\ln I_T$ vs T^{-1} for argon-saturated toluene suspensions of species *k*.

380 The PL of TDSiNPs suspensions shows the contribution of
 381 two emitting species (*a* and *b* in Figure 3A,B). The observed
 382 wide PL bands (fwhm of about $\Delta E \approx 400$ meV) extending over
 383 the 350–450 nm range and decay lifetimes in the nanosecond
 384 regime are in agreement with those reported for 1 nm size
 385 SiNPs.^{8,9,35} On the assumption that the observed luminescence
 386 is controlled by quantum confinement, particle sizes of 1.3–1.6
 387 nm are estimated from theoretical correlations of the EG with
 388 size reported for H-terminated crystalline SiNPs,⁷ in line with
 389 experimentally determined values (vide supra). The PL of PA-
 390 TDSiNPs also shows two contributing species (*c* and *d* in
 391 Figure 3A,B) with red-shifted PL compared to those of *a* and *b*.
 392 Since PA-TDSiNPs and TDSiNPs mainly differ in their surface
 393 composition ($\equiv\text{Si}-\text{CH}_2-\text{CH}_2-\text{CH}_2-\text{NH}_2$ and $\equiv\text{Si}-\text{NH}-$
 394 $\text{CH}_2-\text{CH}=\text{CH}_2$ surface groups in place of $\equiv\text{Si}-\text{H}$), the
 395 observed differences in their excitation–emission matrix may
 396 only be attributed to the strong dependence of the PL on the
 397 surface chemical composition. Recent theoretical and exper-
 398 imental studies indicate that coverage of SiNPs with alkyl-
 399 groups (Si–C) results in a minimal change in PL spectra.
 400 Since SiNPs with Si–N terminations exhibit significant PL
 401 shifts compared to H-passivated SiNPs,^{27,36} the observed
 402 differences may be attributed to Si–N surface bonds.

403 On the other hand, the PL and PLE spectra of amorphous
 404 BUSiNPs (*e* and *f* in Figure 3C,D) are shifted to the red with
 405 respect to those of crystalline TDSiNPs, as expected from
 406 theoretical calculations for amorphous³⁷ and crystalline⁷
 407 particles of similar size. It has been recently reported²⁷ that
 408 H-passivated SiNPs exposed to the surfactant tetraoctylammo-
 409 nium bromide yield PL spectra in the 400 and 450 nm range as
 410 a consequence of the formation of Si–N surface bonds. Since
 411 no evidence on the formation of Si–N environments was
 412 obtained from XPS and FTIR data of BUSiNPs,¹⁶ tetraocty-
 413 lammonium bromide chemisorption to the particle surface is of
 414 no significance under our synthesis conditions. In fact, the PL
 415 of species *e* and *f* is coincident to that reported for 1.5 nm-size
 416 amorphous SiNPs obtained from the electrochemical etching of
 417 amorphous Si films.³⁸ The excitation–emission matrix of
 418 propylamine-surface derivatized BUSiNPs shows the contribu-
 419 tion of two emitting species (*g* and *h* in Figure 3C,D) with
 420 similar PL and PLE spectra to those of species *e* and *f*. Thus,
 421 Si–C and Si–N environments confining BUSiNPs appears

not to significantly affect the overall density of states within the
 capture volume of spatially confined carriers leading to PL in
 amorphous SiNPs.³⁹

Surface oxidized particles of diverse origin (TD and BU
 synthesis) and with different capping groups, mainly SiO_x-
 TDSiNPs, PASiO_x-TDSiNPs, SiO_x-TD'SiNPs, MASiO_x-
 TD'SiNPs, SiO_x-BUSiNPs, and PASiO_x-BUSiNPs, show a
 similar excitation–emission matrix (see Figure 3E,F) and PL
 decay times τ (see Table 2). These observations strongly
 indicate that the excitation–emission matrix shape and PL
 decay times of oxidized SiNPs < 3 nm in size with surface
 Si–O–Si≡ structures does not depend on the particle
 crystalline structure, neither on size nor on further organic
 capping. The presence of surface Si–O–Si≡ structures
 leads to an EG reduction in the order of 0.2–0.4 eV with
 respect to the respective H-passivated TDSiNPs. These
 observations are in line with theoretical studies predicting
 that the addition of a single oxygen atom to the surface of 1 nm
 size H-passivated Si clusters lowers the optical absorption gap
 by fractions of eV when attached in a bridged configuration
 (Si–O–Si) but larger impacts on the EG (units of eV) are
 expected when attached in a double-bonded (>Si=O)
 configuration.^{8,10}

The excitation and emission spectrum of the oxidized
 particles shows peaking with an average peak separation of
 140–180 meV, on the order of the splitting due to zero-
 phonon line and phonon side bands reported in single molecule
 experiments of 5 and 6 nm size oxidized crystalline SiNPs
 embedded in a matrix.^{40–43} Energy spacing close to 150 meV
 may be attributed to Si–O–Si longitudinal optical (LO) and
 transverse optical (TO) phonons at the interface.⁴¹ Assuming
 an electron–phonon interaction, the higher energy of the zero
 phonon line observed herein (>3.0 eV) might correlate with
 the smaller silicon core size of the particles in a quantum
 confinement regime but seems not to support a strong
 localization of both the electron and the hole at the interface
 as suggested by the observed independence on particle size and
 crystallinity.⁴² Since effects as the compressive strain exerted by
 the matrix on embedded nanocrystals may also influence Si-
 NPs PL,⁴⁴ any discussion on the origin of the observed
 differences requires the comparison with single molecule
 experiments with the ultrasmall blue emitting SiNPs.

Overall, the obtained results strongly indicate that for small structures where the number of surface atoms is a significant fraction of the total number of atoms (see S.I. Surface Si atoms estimation (Supporting Information)), different adsorbates and atomic arrangements lead to different surface electronic states which influence the SiNPs PL. SS variations of crystalline SiNPs have been largely attributed to energy levels below the conduction band minimum leading to self-trapped excitons localized in the surface. Such deep levels were reported to be introduced by surface states, dangling bonds, and electron–phonon interactions.⁴⁵ Interestingly, Figure 4A shows an acceptable correlation between the SS and the EG for the different emitting species. These observations and the fact that the same transition is involved in the absorption and emission processes (vide supra) strongly support the contribution of surface states to the energy levels in the gap. It should be noted that species *d* and *h* contributing to PA-TDSiNPs and PA-BUSiNPs, respectively, are an exception. Chemisorbed N may introduce additional deep levels below the conduction band minimum not affecting the EG. Unfortunately, determination of the precise nature of the contributing species is not possible, and the data is usually open to various interpretations.

Larger SiNPs (>2 nm size) explored in the literature showing green to near-IR PL originated in net quantum confinement effects^{44,46,47} are also reported to show important modifications in the PL upon changes in their surface chemistry.^{48–50} Therefore, the participation of surface states in SiNPs PL exceeds our observations for small silicon nanoparticles with large surface to volume ratios.

Temperature Dependence of the Emission Quantum Yield. The overall luminescence quantum yield of argon-saturated toluene suspensions of the particles diminish with increasing temperature, as shown for MASiO_x-TD/SiNPs in S.I. Table 1 (Supporting Information). The Φ values are fully recovered upon restoring the temperature to the initial values, thus supporting reversible temperature-dependent quenching processes. Plots of $\ln(\Phi^{-1} - 1)$ vs T^{-1} show curvature, as expected if two or more deactivation processes with significant activation energies are present. In fact, Φ values cannot separate the individual contributions of all the emitting species. Therefore, to understand the temperature effect on PL, a bilinear analysis of the excitation–emission obtained at each temperature in the range from 273 to 330 K was performed for all the particle samples. Such analysis indicates that the intensity but neither the EG nor the SS of each contributing species depends on temperature. Figure 4B shows the decrease of I_T/I_{273} with temperature for several of the contributing species. The ratio of total intensity at a given temperature *T* with respect to that observed at 273 K (I_T/I_{273}) was used to compensate for all non-temperature-dependent parameters affecting I_T as those of the equipment response and particle concentration. Except for those of species *d*, I_T/I_{273K} values fall within the same curve, therefore suggesting that the thermally activated quenching does not show a correlation with the particle structure and surface chemistry. Interestingly, τ values showed no variation, within the experimental error, in the 200–330 K temperature range.

Calcott's model assuming a thermal equilibrium between two excitonic levels of different multiplicity and radiative constant, split by energy (ΔE), is widely used in the literature to interpret the dependence with temperature of the radiative rate constant k_r .^{13,14,51–53} At very low temperatures, almost all of the excitons are trapped in the lower state, whereas at higher temperatures,

the excitons are in their upper state which is a dominant luminescent center. Reported ΔE values are on the order of 3 meV.^{13,52} Considering that k_r is expected not to vary with temperature for $T > 200$ K, decreasing PL intensities with increasing temperature have been attributed to the dominating role of nonradiative recombination.^{13,54} Two main models were postulated to account for nonradiative thermally activated processes: a normal Arrhenius behavior^{13,55} and the ionization of the excited state via tunneling through a potential barrier with a Berthelot-type *T*-dependence.^{54,56–58} However, considering that our results show that $(k_r + \sum_i k_{ni}) = \tau^{-1}$ remains constant with temperature, k_r being itself *T*-independent, competing nonradiative processes $\sum_i k_{ni}$ originated in the excitonic level are also expected to be temperature independent. Therefore, the involvement of any of the described mechanisms cannot describe the observed *T*-dependence of the PL intensity.

A static, reversible, thermal quenching of the particles is strongly suggested. Increasing temperatures lead to an increased population of nonemitting particles which might be reverted upon a decrease in temperature. Moreover, since no correlation between the quenching rate and the particle surface chemistry is observed, it is expected that the silicon structure is involved in leading to dark (nonemitting) clusters. These observations are in agreement with those by Diener and co-workers⁵⁹ indicating that IR excitation of porous silicon results in a drop in the PL intensity but only with a slight change in the PL lifetime. The authors suggested that IR excitation creates additional dangling bonds or opens additional nonradiative channels leading to an increase of the fraction number of dark crystallites.

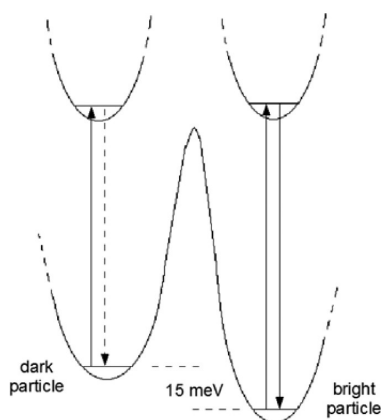
Plots of $\ln I_T$ vs T^{-1} (see inset in Figure 4B) yield straight lines from which the slopes of the enthalpy change $\Delta H = +(15 \pm 1)$ meV of the thermal process leading to the dark particle conformation may be obtained. The observed energy difference between a bright and a dark particle is too small to be assigned to the generation of dangling bonds and are thus suggested to be due to small changes in the structure conformation.

Literature reports on the presence of a dark fraction of particles in quantum dots have been related to blinking dynamics.⁶⁰ Reported single molecule level PL studies with Si nanocrystals revealed PL blinking with power-law statistics and “on” and “off” times in the millisecond–second range.⁶¹ Strong disorder effects were reported to provoke the reversible bleaching of SiNPs on a time scale of hours in the dark.⁶¹ A photogeneration mechanism of the dark particles would imply a reduction in the intensity of steady-state PL with the irradiation time. Since no changes in the steady state PL intensity were observed with the illumination time for the particles herein synthesized, dark SiNPs might be assumed in equilibrium with bright particles before illumination. Scheme 3 illustrates the thermal process between dark and bright particles leading to an increased fraction of dark particles as temperature increases. If power-law statistics of blinking also holds for our SiNPs, then it could arise from a multiplicity of dark (or bright) conformations with different energy barriers.

CONCLUSION

Important challenges in the use of SiNPs as sensors and photosensitizers are the following: their PL dependence on size, crystallinity, and surface structure and chemistry. Also, the low stability of H-terminated SiNPs leads to unwanted surface-oxidized particles unless the synthesis process and surface

Scheme 3. Illustration of the Thermal Process Involving Dark and Bright SiNPs (not scaled)^a



^aArrows stand for radiative (solid) and non-radiative (dashed) processes.

589 derivatization are performed under strict oxygen-free con-
 590 ditions. Our results show that the PL properties of mild surface
 591 oxidized 1–2 nm sized particles mainly showing Si—O—Si
 592 bridging bonds are independent of the synthesis procedure (BU
 593 or TD) and on the further derivatization of the particles surface
 594 with organic molecules with different terminal groups. This
 595 observation has important consequences for the particles’
 596 technological uses as the proper synthesis route may be selected
 597 on costs and availability of reactants and equipment. Moreover,
 598 even though the main synthetic procedure requires minimiza-
 599 tion of the dissolved O₂, further silanization procedures for
 600 organic capping may be conducted under an air atmosphere at
 601 room temperature. As a result, biocompatible molecules may be
 602 attached to the surface without changes in the PL. The latter
 603 properties are important for specific targeting and opsonin
 604 association prevention in sensing applications.

■ ASSOCIATED CONTENT

● Supporting Information

607 TEM, XPS, and FTIR data. This material is available free of
 608 charge via the Internet at <http://pubs.acs.org>.

■ AUTHOR INFORMATION

Corresponding Author

611 *E-mail: gonzalez@inifta.unlp.edu.ar (M.C.G.).

Present Address

613 [§]Department of Chemistry and Biochemistry, Center for
 614 Bioenergy and Photosynthesis, Arizona State University,
 615 Tempe, Arizona 85287–1604, USA (M.J.L.-P.).

Notes

617 The authors declare no competing financial interest.

■ ACKNOWLEDGMENTS

619 M.J.L.-P and J.J.R. thank Consejo Nacional de Investigaciones
 620 Científicas y Técnicas (CONICET, Argentina) for graduate
 621 studentships. M.C.G., M.L.D, and H.B.R. are research members
 622 of CONICET, Argentina. This research was supported by the
 623 grant PIP 112-200801-00356 from CONICET. The authors
 624 grateful for the use of facilities within the LeRoy Eyring Center
 625 for Solid State Science at Arizona State University for TEM
 626 micrographs. M.J.L.-P. and A.L.M are grateful to the Center for
 627 Bio-Inspired Solar Fuel Production an Energy Frontier

Research Center funded by the U.S. Department of Energy, 628
 Office of Science, Office of Basic Energy Sciences, for the 629
 Award Number DE-SC0001016. 630

■ REFERENCES

- 631
- (1) Llansola Portolés, M. J.; Rodriguez Nieto, F.; Soria, D. B.; 632
 Amalvy, J. I.; Peruzzo, P. J.; Mártire, D. O.; Kotler, M. L.; Holub, O.; 633
 Gonzalez, M. C. *J. Phys. Chem. C* **2009**, *113*, 13694. 634
 - (2) Llansola Portolés, M. J.; David Gara, P. M.; Kotler, M. L.; 635
 Bertolotti, S.; San Román, E.; Rodríguez, H. B.; Gonzalez, M. C. 636
Langmuir **2010**, *26*, 10953. 637
 - (3) Popplewell, J. F.; King, S. J.; Day, J. P.; Ackrill, P.; Fifield, L. K.; 638
 Cresswell, R. G.; di Tada, M. L.; Liu, K. J. *Inorg. Biochem.* **1998**, *69*, 639
 177. 640
 - (4) Park, J.-H.; Gu, L.; von Maltzahn, G.; Ruoslahti, E.; Bhatia, S. N.; 641
 Sailor, M. J. *Nat. Mater.* **2009**, *8*, 331. 642
 - (5) Yu, M. K.; Park, J.; Jon, S. *Theranostics* **2012**, *2*, 42. 643
 - (6) Eckhoff, D. A.; Sutin, J. D. B.; Clegg, R. M.; Gratton, E.; 644
 Rogozhina, E. V.; Braun, P. V. *J. Phys. Chem. B* **2005**, *109*, 19786. 645
 - (7) Delley, B.; Steigmeier, E. F. *Appl. Phys. Lett.* **1995**, *67*, 2370. 646
 - (8) Draeger, E. W.; Grossman, J. C.; Williamson, A. J.; Galli, G. J. 647
Chem. Phys. **2004**, *120*, 10807. 648
 - (9) Dai, Y.; Han, S.; Dai, D.; Zhang, Y.; Qi, Y. *Solid State Commun.* 649
2003, *126*, 103. 650
 - (10) Puzder, A.; Williamson, A. J.; Grossman, J. C.; Galli, G. J. *Am.* 651
Chem. Soc. **2003**, *125*, 2786. 652
 - (11) Huang, W.-Q.; Huang, Z.-M.; Cheng, H.-Q.; Miao, X.-J.; Shu, 653
 Q.; Liu, S.-R.; Qin, C.-J. *Appl. Phys. Lett.* **2012**, *101*, 171601. 654
 - (12) Takeoka, S.; Fujii, M.; Hayashi, S. *Phys. Rev. B* **2000**, *62*, 16820. 655
 - (13) Orii, T.; Hirasawa, M.; Seto, T.; Aya, N.; Onari, S. *Eur. Phys. J. D* 656
2003, *24*, 119. 657
 - (14) Lüttjohann, S.; Meier, C.; Offer, M.; Lorke, A.; Wiggers, H. *EPL* 658
(Europhys. Lett.) **2007**, *79*, 37002. 659
 - (15) *Principles of Fluorescence Spectroscopy*, 3rd ed.; Lakowicz, J. R., 660
 Ed.; Springer: Singapore, 2006. 661
 - (16) Llansola Portolés, M. J.; Pis Diez, R.; Dell’Arciprete, M. L.; 662
 Caregnato, P.; Romero, J. J.; Mártire, D. O.; Azzaroni, O.; Ceolín, M.; 663
 Gonzalez, M. C. *J. Phys. Chem. C* **2012**, *116*, 11315. 664
 - (17) Warner, I. M.; Christian, G. D.; Davidson, E. R.; Callis, J. B. 665
Anal. Chem. **1977**, *49*, 564. 666
 - (18) Li, Z. F.; Ruckenstein, E. *Nano Lett.* **2004**, *4*, 1463. 667
 - (19) Caregnato, P.; Forbes, M. D. E.; Soria, D. B.; Mártire, D. O.; 668
 Gonzalez, M. n. C. *J. Phys. Chem. C* **2010**, *114*, 5080. 669
 - (20) Caregnato, P.; Dell’Arciprete, M. L.; Gonzalez, M. C. *Photochem.* 670
Photobiol. Sci. **2013**, DOI: 10.1039/C3PP50067E. 671
 - (21) Huysken, F.; Hofmeister, H.; Kohn, B.; Laguna, M. A.; Paillard, 672
V. Appl. Surf. Sci. **2000**, *154–155*, 305. 673
 - (22) Baldwin, R. K.; Pettigrew, K. A.; Ratai, E.; Augustine, M. P.; 674
 Kauzlarich, S. M. *Chem. Commun.* **2002**, *0*, 1822. 675
 - (23) Launer, J. P. *MRS Bull.* **1997**, *22*, 5. 676
 - (24) Wahab, M. A.; Kim, I.; Ha, C.-S. *J. Solid State Chem.* **2004**, *177*, 677
 3439. 678
 - (25) Soto, G.; Samano, E. C.; Machorro, R.; Cota, L. *Vac. Sci.* 679
Technol. **1998**, *16*, 1311–1315. 680
 - (26) *Silicon-Based Material and Devices*; Nalwa, H. S., Ed.; Academic 681
 Press: San Diego, 2001. 682
 - (27) Dasog, M.; Yang, Z.; Regli, S.; Atkins, T. M.; Faramus, A.; Singh, 683
 M. P.; Muthuswamy, E.; Kauzlarich, S. M.; Tilley, R. D.; Veinot, J. G. 684
C. ACS Nano **2013**, *7*, 2676. 685
 - (28) Zhou, S.; Liu, W.; Cai, C.; Liu, H. Comparative investigation of 686
 infrared optical absorption properties of silicon oxide, oxynitride and 687
 nitride films. *Proceedings of SPIE 7995, Seventh International Conference* 688
on Thin Film Physics and Applications, 2010; 79950T; doi: 10.1117/ 689
 12.88194. 690
 - (29) Vandenberg, E. T.; Bertilsson, L.; Liedberg, B.; Uvdal, K.; 691
 Erlandsson, R.; Elwing, H.; Lundström, I. J. *Colloid Interface Sci.* **1991**, 692
147, 103. 693

- 694 (30) Naviroj, S.; Koenig, J. L.; Ishida, H. *J. Macromol. Sci., Part B*
695 **1983**, 22, 291.
- 696 (31) Wang, P. W.; Bater, S.; Zhang, L. P.; Ascherl, M.; Craig, J. H., Jr.
697 *Appl. Surf. Sci.* **1995**, 90, 413.
- 698 (32) Ouyang, M.; Yuan, C.; Muisener, R. J.; Boulares, A.; Koberstein,
699 J. T. *Chem. Mater.* **2000**, 12, 1591.
- 700 (33) Kluth, G. J.; Sung, M. M.; Maboudian, R. *Langmuir* **1997**, 13,
701 3775.
- 702 (34) Garrido, B.; Lopez, M.; Gonzalez, O.; Perez-Rodriguez, A.;
703 Morante, J. R.; Bonafos, C. *Appl. Phys. Lett.* **2000**, 77, 3143.
- 704 (35) Smith, A.; Yamani, Z. H.; Roberts, N.; Turner, J.; Habbal, S. R.;
705 Granick, S.; Nayfeh, M. H. *Phys. Rev. B* **2005**, 72, 205307.
- 706 (36) Tu, C.-C.; Hoo, J.-H.; Böhringer, K. F.; Lin, L. Y.; Cao, G. *Opt.*
707 *Lett.* **2012**, 37, 4771.
- 708 (37) Park, N.-M.; Choi, C.-J.; Seong, T.-Y.; Park, S. J. *Phys. Rev. Lett.*
709 **2001**, 86, 1355.
- 710 (38) Xie, Y.; Wu, X. L.; Qiu, T.; Chu, P. K.; Siu, G. G. *J. Cryst. Growth*
711 **2007**, 304, 476.
- 712 (39) Estes, M. J.; Moddel, G. *Phys. Rev. B* **1996**, 54, 14633.
- 713 (40) Saar, A. *J. Nanophotonics* **2009**, 3, 032501.
- 714 (41) Martin, J.; Cichos, F.; Huisken, F.; von Borczyskowski, C. *Nano*
715 *Lett.* **2008**, 8, 656.
- 716 (42) El-Kork, N.; Huisken, F.; Borczyskowski, C. v. *J. Appl. Phys.*
717 **2011**, 110, 074312.
- 718 (43) Schmidt, T.; Chizhik, A. I.; Chizhik, A. M.; Potrick, K.; Meixner,
719 A. J.; Huisken, F. *Phys. Rev. B* **2012**, 86, 125302.
- 720 (44) Kusova, K.; OndiC, L.; Klimesova, E.; Herynkova, K.; Pelant, I.;
721 Danis, S.; Valenta, J.; Gallart, M.; Ziegler, M.; Honerlage, B.; Gilliot, P.
722 *Appl. Phys. Lett.* **2012**, 101, 143101.
- 723 (45) Pan, L.; Sun, Z.; Sun, C. *Scr. Mater.* **2009**, 60, 1105.
- 724 (46) Meier, C.; Gondorf, A.; Luttmann, S.; Lorke, A.; Wiggers, H. J.
725 *Appl. Phys.* **2007**, 101, 103112.
- 726 (47) Hessel, C. M.; Henderson, E. J.; Veinot, J. G. C. *Chem. Mater.*
727 **2006**, 18, 6139.
- 728 (48) Hua, F.; Erogbogbo, F.; Swihart, M. T.; Ruckenstein, E.
729 *Langmuir* **2006**, 22, 4363.
- 730 (49) Li, X.; He, Y.; Swihart, M. T. *Langmuir* **2004**, 20, 4720.
- 731 (50) Dasog, M.; Veinot, J. G. C. *Phys. Status Solidi A* **2012**, 209, 1843.
- 732 (51) Calcott, P. D. J.; Nash, K. J.; Canham, L. T.; Kane, M. J.;
733 Brumhead, D. J. *Phys.: Condens. Matter* **1993**, 5, L91.
- 734 (52) Brongersma, M. L.; Kik, P. G.; Polman, A.; Min, K. S.; Atwater,
735 H. A. *Appl. Phys. Lett.* **2000**, 76, 351.
- 736 (53) Cha, D.; Shin, J. H.; Song, I.-H.; Han, M.-K. *Appl. Phys. Lett.*
737 **2004**, 84, 1287.
- 738 (54) Chao, Y.; Houlton, A.; Horrocks, B. R.; Hunt, M. R. C.;
739 Poolton, N. R. J.; Yang, J.; Siller, L. *Appl. Phys. Lett.* **2006**, 88, 263119.
- 740 (55) Street, R. A. *Philos. Mag. B* **1978**, 37, 35.
- 741 (56) Kapoor, M.; Singh, V. A.; Johri, G. K. *Phys. Rev. B* **2000**, 61,
742 1941.
- 743 (57) Rinnert, H.; Vergnat, M. *Phys. E* **2003**, 16, 382.
- 744 (58) Chao, Y. In *Comprehensive Nanoscience and Technology*;
745 Andrews, D., Sholes, G., Wiederrecht, G., Eds.; Academic Press:
746 Amsterdam, 2011.
- 747 (59) Diener, J.; Ben-Chorin, M.; Kovalev, D. I.; Ganichev, S. D.;
748 Koch, F. *Thin Solid Films* **1996**, 276, 116.
- 749 (60) Durisic, N.; Wiseman, P. W.; Grütter, P.; Heyes, C. D. *ACS*
750 *Nano* **2009**, 3, 1167.
- 751 (61) Martin, J.; Cichos, F.; Chan, I. Y.; Huisken, F.; Borczyskowski,
752 C. V. *Israel J. Chem.* **2004**, 44, 341.